Internal motion time scales of a small, highly stable and disulfide-rich protein: A ^{15}N, ^{13}C NMR and molecular dynamics study

Marc Guenneugues*, Bernard Gilquin, Nicolas Wolff, André Ménez & Sophie Zinn-Justin**
CEA, Département d'Ingénierie et d'Etudes des Protéines, CE Saclay, F-91191 Gif-sur-Yvette Cedex, France

Abstract

Motions of the backbone $C_\alpha H_\alpha$ and threonine $C_\beta H_\beta$ bonds of toxin α were investigated using natural abundance ^{13}C NMR and molecular dynamics. Measurement of the ^{13}C longitudinal and transverse relaxation rates employed ACCORDION techniques together with coherence selection by pulsed field gradients and sensitivity enhancement through the use of preservation of equivalent pathway, thus allowing a considerable reduction of the required spectrometer time. ^{13}C R_1, R_2, ^{1}H→^{13}C NOE were obtained, as well as the variations of $R_{1\rho}(90°)$ as a function of the rf field strength. These data were compared to those recorded by ^{1}H and ^{15}N NMR on a labelled sample of the toxin [Guenneugues et al. (1997) *Biochemistry*, **36**, 16097–16108]. Both sets of data showed that picosecond to nanosecond time scale motions are well correlated to the secondary structure of the protein. This was further reinforced by the analysis of a 1 ns molecular dynamics simulation in water. Several $C_\alpha H_\alpha$ and threonine $C_\beta H_\beta$ experimentally exhibit fast motions with a correlation time longer than 500 ps, that cannot be sampled along the simulation. In addition, the backbone exhibits motions on the microsecond to millisecond time scale on more than half of its length. Thus, toxin α, a highly stable protein ($T_m = 75\,°C$ at acidic pH) containing 61 amino acids and 4 disulfides, shows important internal motions on time scales ranging from 0.1–0.5 ps, to 10–100 ps, 1 ns, and about 30 μs to 10 ms.

Abbreviations: BPTI, bovine pancreatic trypsin inhibitor; Ea, erabutoxin a; Eb, erabutoxin b; HSQC, heteronuclear single quantum correlation; NOE, nuclear Overhauser effect; TOCSY, total correlation spectroscopy; TPPI, time proportional phase increment.

Introduction

Average three-dimensional structures obtained either by X-ray crystallography or by NMR spectroscopy often do not completely explain the biological observations, nor do they necessarily provide all the information required for protein engineering or drug

design. Protein function, in many cases, implies conformational changes, and hence is critically dependent on flexibility. Heteronuclear magnetic resonance spectroscopy has been widely used in the recent past for the characterisation of protein motions, in order to better describe the role of these motions in various biological functions (Kay, 1998). The relationship between stability and flexibility was investigated on mutants of BPTI (Wüthrich et al., 1980; Beeser et al., 1997). The authors showed that the rate of ring flipping and methyl dynamics in the hydrophobic core are not clearly enhanced in less stable mutants, but that microsecond time scale motions are more important and concern about one third of the residues in Y35G BPTI. Consistently, microsecond time scale motions

were found to be enhanced in the oxidized, and less stable form, of cytochrome b5 when compared to its reduced state (Banci et al., 1998). On another hand, correlations between binding and dynamics at protein-protein interfaces were proposed (Akke et al., 1993; Rishel et al., 1994; Kay et al., 1998). Increased rigidity upon ligand binding was shown to affect only protein loops adjacent to the ligand (Akke et al., 1993), or a much larger number of residues (Rishel et al., 1994). Furthermore, Kay et al. (1998) proposed, on the basis of the analysis of methyl group motions in SH_2 domains free or complexed to their targets, that differences in binding affinities which cannot be accounted for by static pictures of the interaction, may reflect the influence of dynamics on the van der Waals contribution to the binding energy.

All these results rely on a detailed description of backbone and side-chain dynamics. From an experimental point of view, the most complete description of backbone dynamics was obtained by combining NMR data that monitor the motions of NH and $C_\alpha H_\alpha$ or $C'C_\alpha$ vectors (LeMaster and Kushlan, 1996; Wand et al., 1996; Fischer et al., 1997; Zhu et al., 1998). Side-chain dynamics were also studied using ^{13}C and ^2H NMR relaxation measurements (Nicholson et al., 1992; LeMaster and Kushlan, 1996; Engelke and Rüterjans, 1998; Kay et al., 1998). Amplitudes of the backbone NH, $C_\alpha H_\alpha$ or $C'C_\alpha$ and side-chain CH motions were extracted from the NMR data using one of the two common approaches, model-free analysis (Lipari and Szabo, 1982a,b) or spectral density mapping (Peng and Wagner, 1992a,b; Farrow et al., 1995; Ishima and Nagayama, 1995; Lefèvre et al., 1996). However, a comprehensive atomic description of the protein motions is not accessible by NMR. Thus, molecular dynamics simulations have provided structural models over time to aid in the interpretation and representation of the experimental data (Palmer, 1993; Fushman et al., 1994; Smith et al., 1995; Wong and Daggett, 1998).

In this paper, we report the first extensive joint analysis of the backbone ^{15}NH and $^{13}C_\alpha H_\alpha$ motions of a protein, the 61 amino acid toxin α, by NMR and molecular dynamics. The snake toxin α from *Naja nigricollis* belongs to the α-neurotoxin family, composed of antagonists of the nicotinic acetylcholine receptor. Its three-dimensional solution structure was solved on the basis of ^1H NMR data (Zinn-Justin et al., 1992). Toxin α folds into three major loops stabilized by four disulfide bridges. Characterization of its backbone $C_\alpha H_\alpha$ motions on the basis of natural abundance

^{13}C NMR data is presented. The results are compared to the previously reported description of the backbone NH motions on a picosecond to millisecond time scale, based on ^{15}N relaxation rates measurements (Guenneugues et al., 1997; Zinn-Justin et al., 1997). The observed agreement between the ^{15}N, ^{13}C NMR derived and simulated amplitudes of the picosecond to nanosecond time scale motions allowed the validation of the molecular dynamics trajectory. A combined use of the experimental and simulated information enabled the extension of the NMR relaxation data interpretation, leading to the description of the different time scales of the picosecond to millisecond time scale motions in toxin α. In particular, the presence of internal motions on a time scale longer than 100 ps for backbone and side-chain CH bonds, and the existence of microsecond to millisecond time scale motions in the major part of the backbone are demonstrated. Thus, large amplitude motions are not restricted to the functional site of toxin α, but are found in the whole protein.

Materials and methods

NMR experimental conditions

Toxin α was purified from *Naja nigricollis* venom (Institut Pasteur, Paris) as described previously (Fryklund and Eaker, 1975). Toxin α (14 mg) was dissolved in 400 μl of D_2O at pD 3.5, so that the final concentration was 5 mM.

The complete ^1H assignment and the three-dimensional structure in solution of toxin α were determined previously by Zinn-Justin et al. (1992). ^{13}C chemical shift assignment was performed on the basis of the known ^1H chemical shifts, and confirmed by analysing an HSQC-TOCSY spectrum (Otting and Wüthrich, 1988).

All experiments were acquired at 35 °C on a Bruker DRX500 spectrometer, equipped with a triple-channel probe and three axes pulsed field gradients. For the relaxation studies, data sets consisted of 1024×256 complex points, 64 transients being recorded for each FID. Spectral widths were set to 2000 Hz and 3600 Hz for the ^1H and ^{13}C dimensions, respectively, so as to detect all (C_α, H_α) and threonine (C_β, H_β) correlations. Quadrature detection in the indirect dimension was achieved through the States-TPPI scheme (Marion et al., 1989).
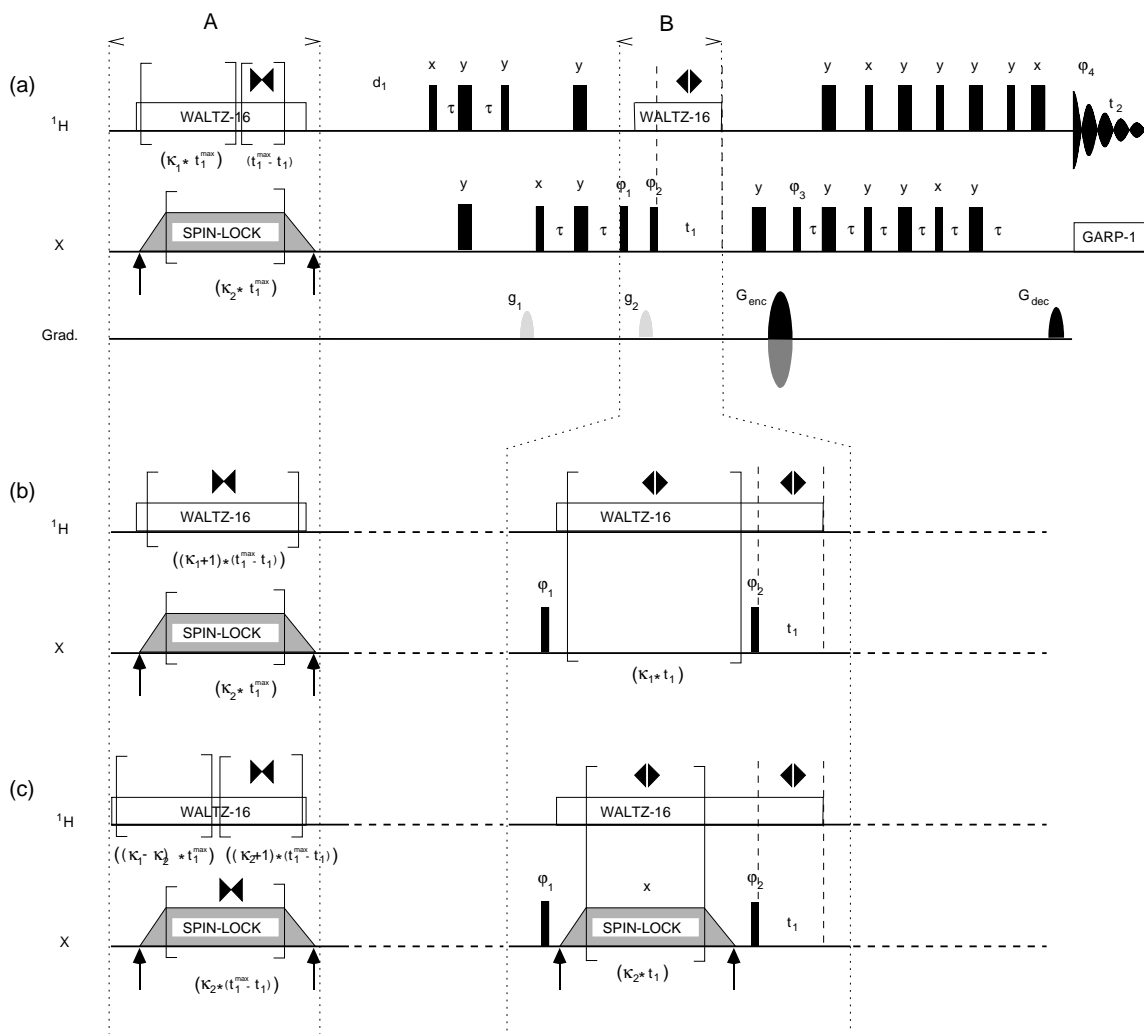
Figure 1. Pulse sequences of the ACCORDION experiments recorded to measure (a) $^{13}C\ R_2^*$, the reference line width, (b) $^{13}C\ R_2^* + k_1 * ^{13}C$ R_1, (c) $^{13}C\ R_2^* + k_2 * ^{13}C\ R_{1\rho}$ (Θ). (a) is a refocused INEPT sequence modified using WALTZ-16 decoupling on the proton channel during t_1; it also includes irradiation periods on the proton and heteronucleus channels before the recovery period so as to ensure a constant delivery power during the entire three experiments. Pulse sequences (b) and (c) are derived from (a) by including an incremented relaxation period of the ^{13}C magnetization prior to the labelling period. Durations of the irradiation pulses preceding the recovery periods are modified accordingly. The recovery delay d_1 is 1.8 s. The narrow and wide solid bars represent 90° and 180° hard pulses, respectively. The hard pulses are centered in the ^1H and ^{13}C spectra. The spin-lock on the heteronucleus is applied through a trapezoidal shape so that the field strength is linearly increased or decreased during 3 ms at the beginning and at the end of the irradiation period. This ensures an adiabatic rotation of the magnetization from the (Oz) axis of the static magnetic field to the (OZ) direction of the effective field and back again. The arrows indicate the positions where the transmitter frequency is changed. The value of τ is set to 1.67 ms. g_1 and g_2 are purged gradients while G_{enc} and G_{dec} denote the encoding and decoding gradients used for coherence selection and thus verifying $|G_{enc}/G_{dec}| = \gamma_{1H}/\gamma_{13C}$. Composite 180° pulses are used for the spin-echo where the encoding and decoding gradients are applied. Two successive experiments with $\varphi_3 = y$ and $-y$ and inverse G_{enc} signs are recorded and rearranged so as to achieve sensitivity enhancement through the preservation of equivalent pathways (Cavanagh et al., 1991). Phase cycling is $\varphi_1 = (y, -y)$, $\varphi_2 = (x, -x)$, $\varphi4 = (x, -x)$. φ_2 is incremented in a States-TPPI manner.

NMR sequences for the evaluation of ^{13}C relaxation rate constants

These sequences are based on the ^{1}H-^{13}C double HSQC (Bodenhausen and Ruben, 1980) recorded with coherence selection by pulsed field gradients (Davis et al., 1992) and with sensitivity enhancement through the use of preservation of equivalent pathway techniques (Palmer at al., 1991a; Kay et al., 1992; Cavanagh and Rance, 1993; Schleucher et al., 1994). GARP-1 (Shaka et al., 1985) and WALTZ-16 (Shaka et al., 1983) were used to decouple ^{13}C spins during the acquisition and ^{1}H spins during the labelling and relaxation periods, respectively (Figure 1).

For the measurement of ^{13}C longitudinal and transverse relaxation rates, the ACCORDION approach was adapted from Bodenhausen and Ernst (1981), and more precisely in the heteronuclear case from Mandel and Palmer (1994). The name of this approach arises from the fact that the duration of an evolution period is varied with t_1 during the experiment. In the present case, the refocused HSQC is modified to include prior to the t_1 labelling delay, a relaxation period (longitudinal or transverse) proportional to t_1. The proportionality constant, the 'accordion factor' k_{rel}, is chosen so that during the experiment (i.e. when t_1 varies from 0 to t_1^{max}), the relaxation behaviour is significantly affected without excessively altering the sensitivity (i.e. $k_{rel} \times t_1$ varies from 0 to 1.5 to 2 times the relaxation time $1/R_{rel}$ being measured). In such an experiment, the linewidth in the ^{13}C dimension depends no longer on R_2^*, but on $R_2^* + k_{rel} \times R_{rel}$. Thus, the recording of a reference and two ACCORDION experiments enables the evaluation of the longitudinal and transverse relaxation rates in about 3.5 days.

The three pulse sequences are displayed in Figure 1. In all sequences, saturation of the ^{1}H frequencies during t_1 was performed in order to interpret the R_2^* values (measured in the reference experiment (a)) as the ^{13}C transverse relaxation rates in the absence of irradiation (Tjandra et al., 1995a; Akke et al., 1998). As these values were found to be equal to the corresponding $R_{1\rho}$ (90°) values within the experimental error for several residues (see below), the effect of B_0 spatial inhomogeneity was neglected. In the following, R_2^* will thus be marked R_2. The ^{13}C transverse relaxation rates in the presence of an off-resonance rf field (Desvaux et al., 1995; Zinn-Justin et al., 1997) were extracted from experiments (a), (b) and (c). Indeed, in experiment (c), the measured rates relate to R_1 and $R_{1\rho}(90°)$ according to:

$$R_{1\rho}(\Theta) = R_1 \times cos^2\Theta + R_{1\rho}(90°) \times sin^2\Theta,$$

Θ being the angle between the effective field and the axis of the static magnetic field. The calculations yielding the $R_{1\rho}$ (90°) values are summarized in the following scheme:

(a) R_2

(b) $R_2 + k_1 \times R_1 \qquad \rightarrow R_1 = (b - a)/k_1$

(c) $R_2 + k_2 \times R_{1\rho}(\Theta) \quad \rightarrow R_{1\rho}(\Theta) = (c - a)/k_2$

$\qquad \rightarrow R_{1\rho}(90°) = [((c - a)/k_2) - cos^2\Theta \times$

$\qquad ((b - a)/k_1)]/sin^2\Theta$

Typically, accordion factors of 7 (k_1) and 3 (k_2), corresponding to maximum relaxation durations $k_{rel} \times t_1^{max}$ of 510 and 220 ms, were chosen for the R_1 and the $R_{1\rho}$ (Θ) measurements, respectively. The recovery delay was set to 1.8 s. All data sets were Fourier-transformed in the ^{1}H dimension after rearrangement of the p/n mixed acquired data (Cavanagh et al., 1991) and application of a 90° shifted sine-bell apodisation function. They were analyzed in the ^{13}C dimension using XWINNMR (Bruker) and in-house FORTRAN software, which enables the determination of the characteristic parameters of correlation peaks (resonance frequency, intensity, linewidth and phase) on extracted slices of the 2D map along ω_1, by fitting to an analytical expression of the frequency domain (Gesmar et al., 1990).

The heteronuclear NOEs were calculated as the ratio of the peak volumes measured on the spectra recorded with and without ^{1}H saturation using the peak integration facility provided in the FELIX program (Molecular Simulations). For the former experiment, a recovery delay followed by a 2.2 s ^{1}H irradiation period was applied. For the latter experiment, the recovery delay was set to 4.2 s. The ^{1}H irradiation was composed of 7 ms spaced 120° pulses. The recording time was 1.5 days for each experiment.

For statistical analysis, the ^{13}C R_1, $R_{1\rho}$ (Θ) and R_2 were measured three, seven and three times, respectively, and the ^{1}H→^{13}C NOEs were measured in duplicate.

Analysis of the ^{15}N and ^{13}C NMR data using spectral density mapping

The values of J(0), J(ω_N), and J(0.87*ω_H) were extracted from the experimental ^{15}N R_1, $R_{1\rho}$ (90°) and ^{1}H→^{15}N NOE data (Farrow et al., 1995; Guenneugues et al., 1997). The values of J(0), J(ω_C), and

(a)

(b)
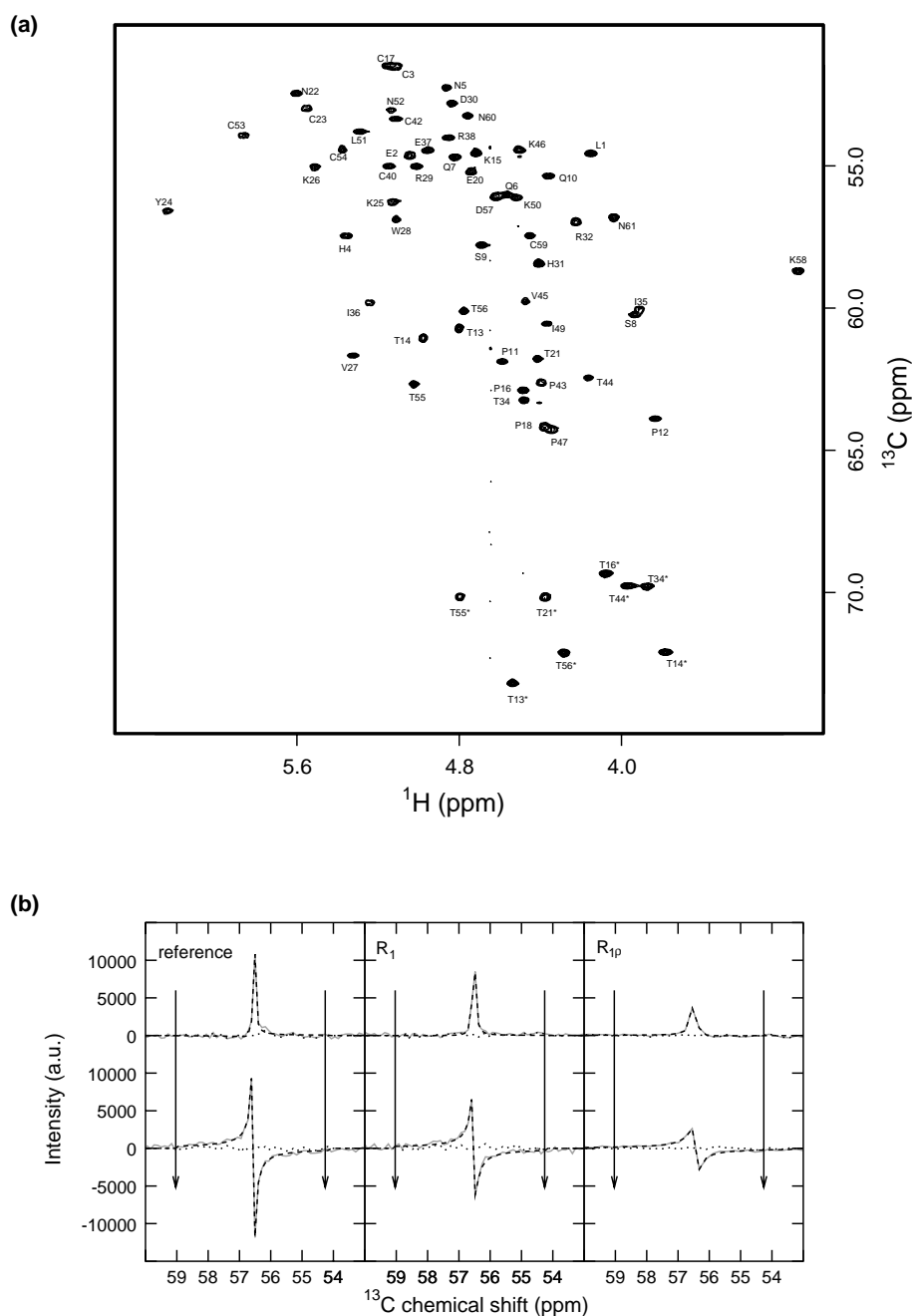
Figure 2. (a) ^{1}H–^{13}C correlated spectrum of toxin α recorded using the sequence described in Figure 1a. Labelling gives the assignment of $C_\alpha H_\alpha$ and $C_\beta H_\beta$ (indicated by asterisks) correlations. The severely overlapping peaks corresponding to Q6, K50 and D57 were not analyzed. (b) 1D slices (real and imaginary parts) along the ^{13}C dimension corresponding to the Y24 $C_\alpha H_\alpha$ correlation, extracted from the spectra recorded using pulse sequences 1a, 1b and 1c for lineshape analysis. The arrows delineate the 400 Hz spectral width used for the fitting. Raw and fitted spectra are displayed in plain gray and dashed black respectively, while the residual is plotted with black dots. The lineshape is broadened in the ACCORDION spectra (20.5 Hz, 39.9 Hz and 61.8 Hz in the reference, R_1 and $R_{1\rho}$ (90°) experiments, respectively).

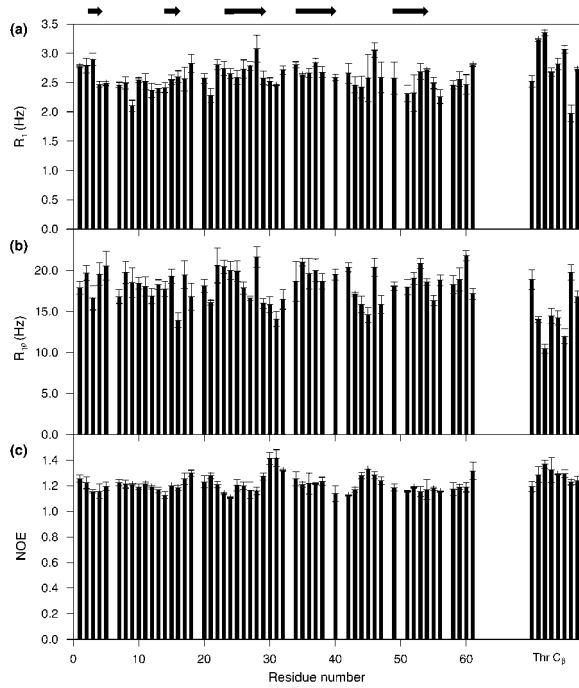*Figure 3.* (a) ^{13}C R_1, (b) ^{13}C $R_{1\rho}$ (90°), (c) ^{1}H→^{13}C NOE values as a function of the sequence. On the x axis, the C_α are numbered as their corresponding residues; the C_β are labelled as 'Thr' and are displayed sequentially (13, 14, 16, 21, 34, 44, 55, 56). Over each graph, bars indicate the positions of the 5 β-strands of toxin α: $β_1$ and $β_2$ in loop 1, $β_3$ and $β_4$ in loop 2, $β_5$ in loop 3.

J(1.56*$ω_H$) were similarly derived from the experimental ^{13}C R_1, $R_{1\rho}$ (90°) and ^{1}H→^{13}C NOE data. All these spectral density values represent the proportion of the total energy used for the motions of a given vector at each corresponding frequency. A comparative analysis of the spectral densities along the sequence thus gives a straightforward view of the distribution of the motion frequencies along the backbone of the molecule. Recently, from the analysis of ^{15}N relaxation data of a series of proteins, Lefèvre et al. (1996) showed that a linear correlation often exists between J(0) on one hand, and J($ω_N$) or J($ω_H$) on the other hand. They proposed that this experimental correlation can be used to identify the different correlation times of protein motions, assuming the spectral density function is a sum of Lorentzians. The spectral density values corresponding to the motions of the NH and CH vectors of toxin α were graphically analyzed in order to discuss the different correlation times of the observed motions.

Analysis of the ^{13}C NMR relaxation data using the Lipari–Szabo formalism

This analysis was performed using Modelfree 3.1 software (Palmer et al., 1991b), which assumes that the molecule tumbles isotropically (even though it may be extended to anisotropic molecules; Tjandra et al., 1995b). Hydrodynamic modeling using HYDRO software (Garcia de la Torre and Bloomfield, 1981; Venable and Pastor, 1988) enabled to estimate an anisotropy of 1.35 and an asymmetry of 1.06 for toxin α (Guenneugues et al., 1997). The overall tumbling of the protein should thus be better described using an axially symmetric model. However, in toxin α, all NH bonds but 8 and all $C_\alpha H_\alpha$ bonds but 10 are perpendicular to the highest component principal axis within ±30°. Thus, as demonstrated for the case of the NH bonds (Guenneugues et al., 1997), the influence of anisotropy on the relaxation data is poor. The isotropic assumption is admitted in the following analyses. In addition, global and internal motions are assumed to be uncorrelated and a hypothesis is made on the shape of the correlation function corresponding to the internal motions. Two models are most currently used. In the first model, the internal motion is assumed to have a unique correlation time, while in the second model two distinct correlation times are considered. The expression of the spectral density function is (Lipari and Szabo, 1982a; Clore et al., 1990):

$$J(\omega) = 2/5[S^2\tau_c/(1 + \omega^2\tau_c^2) + (1 - S^2)\tau_i/(1 + \omega^2\tau_i^2)] \quad (1)$$

with

$$\tau_i^{-1} = \tau_c^{-1} + \tau_e^{-1}$$

and, if $\tau'^{-1}_s = \tau_c^{-1} + \tau_s^{-1}$ and $\tau'^{-1}_f = \tau_c^{-1} + \tau_f^{-1}$,

$$J(\omega) = 2/5[S^2\tau_c/(1 + \omega^2\tau_c^2) + S_f^2(1 - S_s^2)\tau'_s/(1 + \omega^2\tau'^2_s) + \{(1 - S_f^2)\tau'_f/(1 + \omega^2\tau'^2_f)\}] \quad (2)$$

where τ_c is the global rotational correlation time of the protein, τ_e is the unique correlation time of the internal motion in the first model, and τ_s/ τ_f are the correlation times of the slower / faster internal motions in the second model. The braced term in (Equation 2) is neglected provided that τ_f is sufficiently small. Analysis

of the order parameters allows the localisation of the protein regions exhibiting large amplitude motions on the ps–ns time scale.

Furthermore, the direct comparison of R_2 and $R_{1\rho}$ (90°), and the analysis of the variations of $R_{1\rho}$ (90°) as a function of the rf field strength ω_{eff}, enables the detection of protein regions exhibiting slow motions on the µs–ms time scale. Indeed, for a nucleus in slow chemical exchange between two sites of respective populations p_a and p_b and of chemical shift difference $\Delta\omega$, the $R_{1\rho}$ (90°) is altered according to (Deverell et al., 1970; Szyperski et al., 1993):

$$R_{1\rho}(90°) = R_2^{DD,CSA}$$
$$+ p_a p_b (\Delta\omega)^2 [\tau_{ex}/(1 + \omega_{eff}^2 \tau_{ex}^2)],$$

$R_2^{DD,CSA}$ being the transverse relaxation rate due to dipolar interaction and chemical shift anisotropy, τ_{ex} the characteristic time of the exchange process and ω_{eff} the effective field strength upon measurement of the relaxation rate. Knowledge of the variations of $R_{1\rho}$ (90°) as a function of the rf field strength allows the extraction of the $p_a p_b (\Delta\omega)^2$ and τ_{ex} terms corresponding to each nucleus.

Molecular dynamics
A simulation was carried out using CHARMM software (Brooks et al., 1983) and the CHARMM22 parameter set (MacKerell et al., 1998). The toxin average NMR structure (Zinn-Justin et al., 1992), oriented according to its inertia tensor, was used as a starting point. The protein was placed at the center of an equilibrated water box of TIP3 water molecules (Jorgensen, 1981). The box size was set to x = 58 Å, y = 42 Å, z = 32 Å in order to have an initial water density of 0.0333 molecules/Å^3. The final system contained 2221 TIP3 water molecules. The simulation was performed using periodic boundary conditions. A time step of 1 fs was used in conjunction with the SHAKE algorithm (Ryckaert et al., 1977) restraining the length of covalent bonds involving hydrogen atoms. Non-bonded interactions were handled using a 7–12 Å switching function based on neutral groups (Loncharich et al., 1989). After heating and equilibration at 300 K for 10 ps, a trajectory of 1.3 ns was produced. Coordinates were stored every 0.05 ps. The last nanosecond of this trajectory was analyzed in order to compare the amplitudes and time scales of the protein backbone motions that occurred during the simulation to the experimental data. The correlation functions corresponding to the internal motions

were computed and fitted using either a mono (1) or bi-exponential (2) function, corresponding to the Lipari–Szabo formalism in its original and extended forms. They were multiplied by a correlation function corresponding to the global rotational motion of the toxin in order to calculate the spectral density functions J(ω) and compare them to the experimental values.

Results

Measurement of the ^{13}C R_1, $R_{1\rho}(90°)$ and $^1H \rightarrow ^{13}C$ NOE parameters
The resolution of the spectra was high enough to measure ^{13}C relaxation rates for 53 non-glycine C_α and 8 threonine C_β atoms of toxin α (Figure 2). Due to peak overlaps, the errors made on the parameters corresponding to the C_α of Q6, K50 and D57 were significant, so that these data were excluded from our analysis. Average values for ^{13}C R_1, $R_{1\rho}$ (90°) and $^1H \rightarrow ^{13}C$ NOE are displayed in Figure 3. Dependence of the ^{13}C $R_{1\rho}$ (90°) and $^1H \rightarrow ^{13}C$ NOE parameters on the secondary structure is manifest. The highest $R_{1\rho}$ (90°) (about 19 Hz) and the lowest NOEs (about 1.18) match the β-strands fairly well. Analysis of the ^{13}C R_1 (about 2.6 Hz in the β-structure) is more complex. This is probably due to the fact that with a global rotational correlation time of 4 ns (Guenneugues et al., 1997), the internal motions can lower or raise the ^{13}C R_1 value depending on their correlation time. The $R_{1\rho}$ (90°) and NOEs of most threonine C_β are particularly low and high, respectively, indicating that these side chains are at least as mobile as the tip of loop 2 (D30-R32). Standard errors calculated from three independent data sets are lower than 6% for 82% of the R_1 and 93% of the $R_{1\rho}$ (90°), and lower than 5% for 94% of the NOEs.

Estimation of the overall rotational correlation time
The overall rotational correlation time of toxin α in D_2O was derived in an iterative way from the average $R_{1\rho}$ (90°)/R_1 ratio calculated over the residues satisfying criteria adapted from Barbato et al. (1992) and from Tjandra et al. (1995). These criteria were based on: (i) an NOE value lower than the value corresponding to an order parameter of 0.75 at a given τ_c, so as to exclude residues subjected to high amplitude internal motions and (ii) deviations from the average R_1 and $R_{1\rho}$ (90°) values restricted to a range defined by the dependance on τ_c of these parameters, so as to
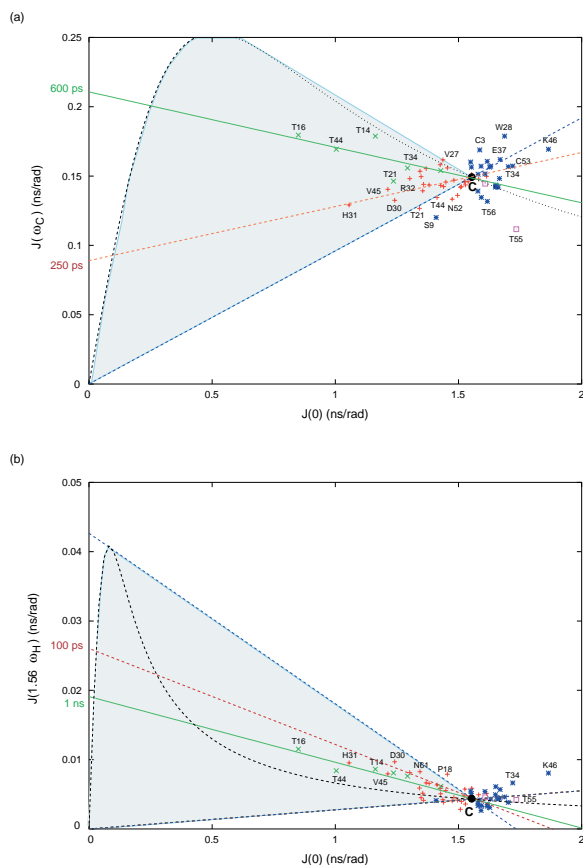
Figure 4. Representation of ^{13}C J(ω_c) (a) and ^{13}C J(1.56*ω_H) (b) as a function of ^{13}C J(0). The dark blue dashed curves show the relationship between the spectral density values at J(0) and J(ω_c or H) when the spectral density is modelled by a Lorentzian. The virtual point C indicates a τ_c of 3.9 ns. The light blue parts of the graphs correspond to regions where the spectral density function can be modelled by a sum of Lorentzians. Experimental points corresponding to C_α are plotted as red crosses when located in the 'allowed' light blue regions, and by blue stars otherwise. Similarly, experimental points corresponding to C_β are displayed as green crosses or pink squares when in or outside the light blue colored region. Residues subjected to internal motions characterized by a unique and common correlation time should be aligned with point C; the green and red lines correspond to different values of this correlation time.

Figure 5. $^{13}C_\alpha$ order parameters as calculated using Modelfree 3.1 (Palmer et al., 1991b). (a) S^2 are plotted as a function of the residue number. (b) S^2 ranges are displayed on a ribbon representation of the toxin structure; residues with S^2 higher than 0.9 are colored in blue, residues with S^2 lower than 0.9 are colored in red; gray indicates residues for which no information is available.

exclude residues subjected to fast exchange without a priori rejecting the effect of the anisotropy. The resulting τ_c value was 3.9 ns, which is slightly higher than the value found in the study of the ^{15}N relaxation data (Guenneugues et al., 1997). This is consistent with the larger viscosity of D_2O compared to H_2O, and was already observed for other proteins (Lee et al., 1997).

Spectral density functions calculated from the ^{13}C relaxation data

In order to characterize the internal motions of the CH bonds, the spectral density function values at frequencies 0, ω_C and 1.56*ω_H were extracted from the NMR relaxation data. J(ω_C) and J(1.56*ω_H) are displayed as a function of J(0) in Figure 4. The blue dashed curves render the dependency of J(ω_C or H) to J(0) when the spectral density function is modelled as a single Lorentzian:

$$
\begin{aligned}
J(\omega) &= 2/5[\tau/(1+\omega^2\tau^2)] = f(\tau) \\
&\Rightarrow J(\omega) = J(0)/(1+\omega^2(2.5J(0))^2) \\
&= g(J(0))
\end{aligned}
$$

First, several CH bonds show J(0) higher than the maximum value $J^{DD,CSA}(0)$, obtained in the absence
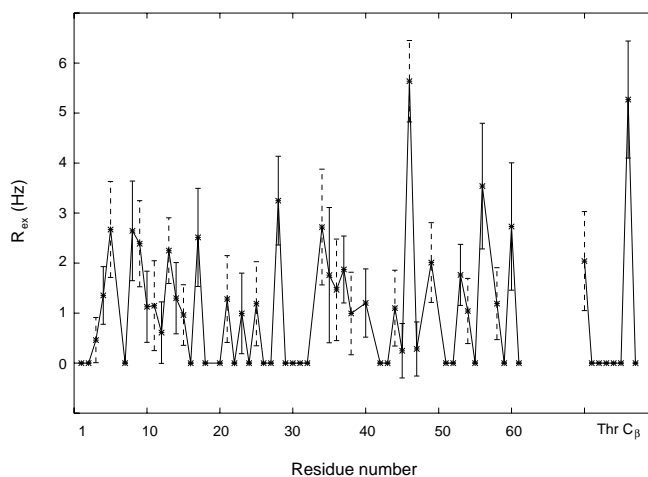
Figure 6. Exchange terms R_{ex} (in Hz) derived from the Modelfree analysis of the $^{13}C_{\alpha}$ relaxation data. On the x axis, the C_{α} are numbered as their corresponding residues; the C_{β} are labelled as 'Thr' and are displayed sequentially (13, 14, 16, 21, 34, 44, 55 and 56).
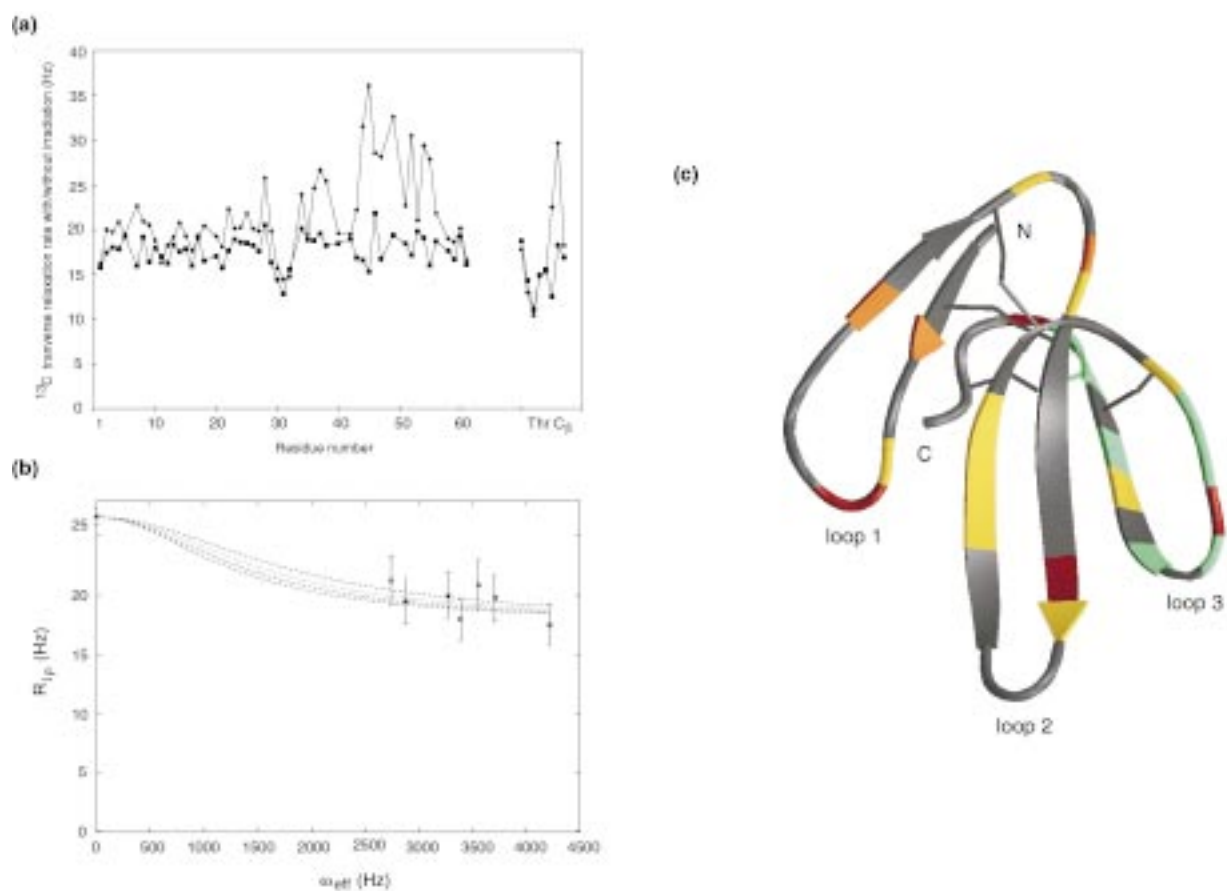
Figure 7. ^{13}C transverse relaxation rates measured at different rf field strengths. (a) Comparison of ^{13}C R_2 (black lines) with ^{13}C $R_{1\rho}$ (90°) (gray lines) as a function of the sequence; in slots 70 to 77 data are plotted for the threonine C_{β}. (b) Variations of the transverse relaxation rate of E37 C_{α} as a function of the rf effective field strength, and fit of the experimental points using time scales varying from 90 to 120 μs. (c) Ranges of slow exchange correlation time of the C_{α} are displayed on a ribbon representation of the toxin structure (red: 30 μs < τ_{ex} < 90 μs, orange: τ_{ex} > 50 μs, yellow: τ_{ex} > 70 μs and $R_2 - R_{1\rho}$ (90°) < 10 Hz, green: τ_{ex} > 70 μs and $R_2 - R_{1\rho}$ (90°) > 10 Hz, gray: no information is available).

of internal motion and corresponding to the overall tumbling correlation time of the toxin ($\tau_c = 3.9$ ns). The virtual point C of Figure 4 corresponds to this value of $J^{DD,CSA}(0)$. As internal motions occurring on a time scale smaller than the overall tumbling can only lead to a decrease of the J(0) value, points with an abscissa value higher than $J^{DD,CSA}(0)$ are subject to fast chemical exchange that we attribute to slow motions on a μs to ms time scale. If we suppose that the spectral density function corresponding to ps to ns time scale motions is a simple sum of Lorentzians, then all the experimental points found outside of the light blue regions of the graphs (Figure 4) correspond to CH bonds exhibiting a μs to ms time scale motion. In particular, Figure 4a shows that the $C_\alpha H_\alpha$ bonds of C3, N5, S8, S9, T13, C17, N22, C23, Y24, K26, W28, T34, I36, E37, C40, C42, K46, I49, L51, C53, C54, T56 and N60 (plotted as blue stars in Figure 4) and the $C_\beta H_\beta$ bonds of T13 and T55 (plotted as pink squares in Figure 4) are subject to these slow motions.

Second, internal motions on a ps to ns time scale tend to increase the value of the spectral density function at higher frequencies and thus to lower it at lower frequencies so that, within the light blue colored region, the experimental points far away from the virtual point C indicate the presence of high amplitude motions on this time scale. In Figure 4a, points reflecting particularly large amplitude internal motions correspond to the $C_\alpha H_\alpha$ bonds of L1 at the N-terminus, Q7 in the turn of loop 1, T16 and T21 just before and after the turn between loops 1 and 2, R29, D30, H31, R32 at the tip of loop 2, V45 in loop 3, T55 in the C-terminal turn, N61 at the C-terminus, and the $C_\beta H_\beta$ bonds of T14, T16, T21, T34 and T44. Additionally, the $C_\alpha H_\alpha$ bond of S9 (tip of loop 1) and the $C_\beta H_\beta$ bond of T55 (C-terminal turn) are found in a region of the graph characteristic of slow exchange and large amplitude fast motions; these points can be moved back to the light blue region (but far away from C) by a simple translation along the J(0) axis, which virtually takes out the contribution of fast exchange from the spectral density function (Figure 4a).

Third, when analyzed in the frame of the Lipari and Szabo model, Figure 4a highlights the correlation time diversity of the internal motions on the ps to ns time scale. Experimental points found in the light blue region of the graph can be approximately divided into those having an internal correlation time around 250 ps (spread along the red line), i.e. the C_α, and those having an internal correlation time around 600 ps (distributed along the green line), i.e. the C_β.
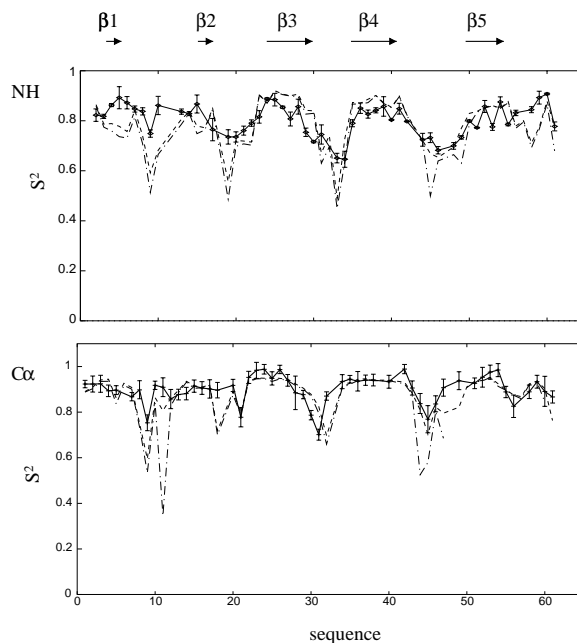
Figure 8. Variations of the backbone NH and $C_\alpha H_\alpha$ order parameters extracted from the NMR data (plain lines) and from the simulation (dashed lines: model 1; dashed dotted lines: model 2).

Interestingly, in Figure 4b, the deduced correlation times for the internal motions are slightly different; they are equal to 100 ps and 1 ns, respectively. This is probably due to two different factors. The approximation $J(\omega_h)=J(\omega_h \pm \omega_c)$ made when calculating the spectral density values leads to a high estimate of $J(\omega_c)$. A low estimate of $J(\omega_c)$ is provided assuming that $J(\omega)$ is proportional to $1/\omega^2$ (Farrow et al., 1995). The correlation time for the internal motions of the $C_\alpha H_\alpha$ bonds is then 50 ps. The exact time scale deduced from the graph of $J(\omega_c)$ as a function of J(0) is thus between 50 ps and 250 ps, which is consistent with the 100 ps value deduced from Figure 4b. In the case of the C_β, the approximations made for the calculation of the spectral density values hardly influence the correlation times deduced from Figures 4a,b. However, the observed discrepancy between Figures 4a and b can be accounted for by taking into account two internal motions per nucleus (see Equation 2). The six green crosses are not well aligned in Figure 4a, but five of them are perfectly aligned with point C in Figure 4b. Thus, in the case of two internal motions, the defined line crosses the blue dashed curve at τ_f and τ_s. τ_s is then close to 1 ns and τ_f to 50 ps (Figure 4b). The misalignment in Figure 4a denotes different values of the order parameters for the fastest motion: T16, T44 and

T21 appear to exhibit ps time scale internal motions with a higher amplitude than T14, T34 and T56.

All these results are consistent with the presence of internal motions over a wide time scale, i.e. around 50–100 ps, 1 ns, and from μs to ms. They also suggest that these three time scales have to be considered to account for some experimental points, as for example those corresponding to the C_β of threonines T13 and T55 exhibiting fast exchange.

Lipari–Szabo analysis of the ^{13}C relaxation data
The ^{13}C R_1, $R_{1\rho}$ (90°) and ^{1}H$\rightarrow$^{13}C NOE were also interpreted using the Modelfree 3.1 program. In this analysis, we mainly used the simplest model of the spectral density function, Equation 1, eventually extended to include a term R_{ex} accounting for contribution to the transverse relaxation of fast chemical exchange arising from μs to ms motions. An order parameter S^2, an internal correlation time τ_e, and a contribution of fast exchange R_{ex} were thus computed by fitting the experimental data. For the 53 C_α and 2 C_β (T13 and T55) data sets, the resulting differences between the observed and modelled relaxation parameters were lower than the experimental errors. For the C_β of threonines 14, 16, 21, 34, 44 and 56, the extended model of the spectral density function, Equation 2, had to be applied. In that case, S_f^2 (the order parameter of the fastest motions), S_s^2 (the order parameter of the slowest motions) and τ_s (the correlation time of the slowest motions, in the 0.1–4 ns range) were fitted to the NMR data. The correlation time of the fastest motions was assumed to be lower than 10 ps and the corresponding term in the spectral density function was neglected.

Amplitudes of ps to ns time scale $C_\alpha H_\alpha$ motions derived from the Modelfree analysis are displayed in Figure 5. The generalized order parameter S^2 varies from 0.70 to 0.99. The error evaluated on this parameter is lower than 0.05 for all the C_α but those of W28, V45 and N60 (errors: 0.06–0.07; see Table 1). Thus, significant variations are observed along the polypeptide chain (Figure 5a). The most rigid regions of toxin α ($S^2 > 0.9$; in blue in Figure 5b) comprise the double-stranded β-sheet of loop 1, the triple-stranded β-sheet stabilizing loops 2 and 3, together with the 8 cystines and 4 of the 5 prolines. Segments not involved in secondary structure elements, like the tips of loops 1 and 2, are more flexible ($S^2 < 0.9$; in red in Figure 5b). Particularly low order parameters ($S^2 < 0.85$; Figure 5a) are found for S9 at the tip of loop 1, T21 in the turn connecting loops 1 and 2, D30, H31 at the tip

of loop 2, T44, V45, K46 in the external part of loop 3, and T56 in the C-terminal turn (Figure 5a). Finally, two C_β of threonines show S^2 values close to those of the backbone C_α: threonines 13 ($S^2 = 0.91$) and 56 ($S_f^2 * S_s^2 = 0.88$). These C_β are even more rigid than the corresponding C_α (Table 1), suggesting that their side chains are involved in stable hydrogen bonds. The 6 other C_β of threonines show S^2 values between 0.45 (T16) and 0.57 (T44): the corresponding C_β are more mobile than any part of the backbone (Table 1).

The internal correlation times τ_e are poorly defined, being significantly higher than 250 ps for only 6 C_α (C3, N22, C23, W28, E37 and K46) amongst 53, but for 5 C_β (T14, T16, T21, T34 and T44) amongst 8 (Table 1). Thus, the NMR data are consistent with the view that most of the $C_\alpha H_\alpha$ bonds experience motions faster than 250 ps, whereas most of the threonine side chains experience at least two types of internal motions, a fast and a slower one (around 1 ns, Table 1).

The contribution to transverse relaxation of μs to ms time scale motions is significant for half of the backbone C_α nuclei (Figure 6). It is particularly important (higher than 1.5 Hz) for N5, S8, S9, T13, C17 in loop 1, W28, T34, E37 in loop 2, K46 in the external part of loop 3, I49, C53 in the β-strand of loop 3, T56 and N60 in the C-terminal loop. In contrast, only two C_β (T13 and T55) exhibit a significant contribution of fast exchange to the transverse relaxation. Surprisingly, the C_α of T55 does not exhibit such a contribution.

We would like to point out the complementarity of the two analyses of the relaxation data presented above. The spectral density mapping gives a qualitative analysis of the protein dynamics which does not depend on any motion models. It points out the presence of particularly high amplitude internal ps to ns motions, or significant μs to ms motions. Moreover, it graphically indicates the simplest model motion consistent with the experimental data. Use of the Modelfree formalism essentially aims at quantifying the parameters describing the internal motions, thus allowing a comparison to the values computed along the simulation for the short time scale motions.

Observation of microsecond to millisecond time scale motions of $C_\alpha H_\alpha$ vectors
The contribution from μs to ms time scale motions to the transverse relaxation is difficult to extract from the sole set of ^{13}C R_1, $R_{1\rho}$ (90°) and ^{1}H$\rightarrow$^{13}C NOE. Identification of carbon sites exhibiting slow motions and estimation of the correlation time of these motions

Table 1. Parameters characterizing the internal motions of toxin α

Res C$_\alpha$	S^2	Std error	τ_e (ps)	Std error	High J(0)	R$_{ex}$ (Hz)	Std error	R$_2$−R$_{1\rho}$	Std error	Var (Hz)	τ_{ex} (μs)	Res NH
1	0.92	0.02	104.741	30.9775		0	0	0.51	0.54	0.51		
2	0.92	0.04	628.107	586.095		0	0	2.63	0.51	2.63		
3	0.92	0.04	1826.77	429.895	*	0.4599	0.4511	1.70	0.87	2.16		120
4	0.89	0.03	12.3943	17.5287		1.3534	0.5774	3.05	0.62	4.40	>50	
5	0.90	0.02	17.211	13.694	*	2.6712	0.9593	0.22	1.11	2.89		<50
7	0.87	0.02	29.3735	10.1491		0	0	6.70	1.12	6.70	>70	
8	0.90	0.04	54.4819	201.378	*	2.6446	0.9967	1.75	1.75	4.39	50–70	
9	0.75	0.03	9.4708	4.4286	*	2.3886	0.8607	4.18	1.42	6.57	50–90	≤50
10	0.92	0.02	18.8994	14.2433		1.1257	0.7116	0.82	1.10	1.95		
11	0.91	0.04	61.6885	199.985		1.1479	0.8983	−0.66	0.30	0.49		
12	0.86	0.04	9.3827	7.6515		0.6094	0.6147	1.99	0.55	2.59		
13	0.88	0.02	3.3882	5.5473	*	2.2492	0.6574	0.80	0.65	3.05		
14	0.88	0.03	7.7705	11.6947		1.2971	0.7125	3.21	0.78	4.51	>50	
15	0.91	0.03	28.7704	23.9872		0.9614	0.6065	1.47	0.94	2.43		
16	0.91	0.03	56.775	193.583		0	0	1.68	1.02	1.68		
17	0.90	0.04	189.25	326.549	*	2.514	0.9806	−0.24	0.93	2.27		20–200
18	0.90	0.03	445.395	203.64		0	0	3.90	1.12	3.90	>70	
20	0.92	0.03	56.7533	41.6375		0	0	2.21	0.88	2.21		135
21	0.78	0.04	31.665	11.8409		1.2803	0.8674	2.33	0.83	3.61	≥50	75
22	0.95	0.03	858.537	597.088	*	0	0	4.66	0.57	4.66	>70	
23	0.98	0.04	1683.71	676.273	*	0.9938	0.8058	1.20	1.32	2.20		
24	0.99	0.02	411.686	683.331	*	0	0	1.69	0.87	1.69		
25	0.95	0.03	194.498	296.987		1.1874	0.841	3.34	1.38	4.53	no fit	
26	0.99	0.02	673.518	764.389	*	0	0	1.85	0.65	1.85		240
27	0.94	0.03	877.061	734.291		0	0	2.24	0.92	2.24		
28	0.88	0.07	1365.78	719.321	*	3.2496	0.8877	5.26	1.17	8.51	40–90	
29	0.88	0.02	93.4308	119.732		0	0	3.47	0.95	3.47	>70	
30	0.79	0.02	86.5776	13.9328		0	0	1.35	0.53	1.35		
31	0.70	0.02	87.4337	9.6721		0	0	1.64	0.77	1.64		
32	0.87	0.02	117.871	32.9647		0	0	−0.83	0.65	−0.83		
34	0.93	0.03	528.578	513.41	*	2.7203	1.1571	3.79	1.53	6.51	no fit	
35	0.94	0.02	53.5732	25.5667		1.76	1.3522	0.58	1.45	2.34		150
36	0.94	0.04	133.69	246.881	*	1.4651	1.0157	5.84	1.15	7.30	>70	
37	0.94	0.02	706.714	368.186	*	1.8731	0.6688	7.08	1.29	8.95	90–120	
38	0.94	0.03	178.526	291.156		0.9925	0.8254	7.16	1.70	8.15	>70	
40	0.93	0.03	33.3832	130.051	*	1.20131	0.6826	1.17	0.89	2.37		
42	0.99	0.02	685.573	526.15	*	0	0	0.53	1.10	0.53		
43	0.91	0.03	43.5271	244.099		0	0	5.33	1.53	5.33	>70	
44	0.84	0.04	55.0219	73.0633		1.0993	0.7584	14.96	1.00	16.06	>70	≥1000
45	0.77	0.06	167.352	285.802		0.2476	0.5438	20.82	1.20	21.06	>70	
46	0.841	0.04	708.946	176.909	*	5.6373	0.8142	6.77	1.76	12.41	50–70	
47	0.911	0.04	119.051	279.059		0.2834	0.5409	11.39	1.68	11.68	>70	
49	0.941	0.04	277.855	553.917	*	2.0106	0.7978	13.24	1.61	15.25	60–120	
51	0.931	0.02	189.275	534.547	*	1	0.9	4.25	1.00	5.25	≥70	290
52	0.951	0.04	427.74	705.23		0	0	13.31	2.08	13.31	>70	
53	0.981	0.03	426.175	629.916	*	1.7637	0.6106	1.22	0.95	2.99		
54	0.981	0.03	242.236	280.177	*	1.0424	0.6513	10.36	1.12	11.40	100–200	

Table 1 (continued)

Res C$_\alpha$	S^2	Std error	τ_e (ps)	Std error	High J(0)	R$_{ex}$ (Hz)	Std error	R$_2$−R$_{1\rho}$	Std error	Var (Hz)	τ_{ex} (μs)	Res NH
55	0.891	0.03	8.775	12.139		0	0	<u>11.85</u>	0.82	<u>11.85</u>	>70	
56	0.831	0.05	6.2745	12.8029	*	<u>3.5401</u>	1.2556	<u>3.17</u>	1.01	<u>6.71</u>	30–60	
58	0.891	0.03	10.5946	14.4836		1.1896	0.719	1.34	0.69	2.53		>1000
59	0.931	0.03	62.0018	254.176		0	0	1.93	0.69	1.93		
60	0.891	0.07	97.4887	267.966	*	<u>2.7317</u>	1.274	0.9	1.39	<u>3.64</u>	no fit	
61	0.871	0.03	230.173	41.8166		0	0	0.56	0.94	0.56		

Thr C$_\beta$	S^2 fast	Std error	S^2 low	Std error	τ_e (ps)	Std error	High J(0)	R$_{ex}$	Std error	R$_2$−R$_{1\rho}$	Std error	Var (Hz)	τ_{ex} (μs)
70	1.00	0.00	0.91	0.04	46.41	229.45	*	<u>2.04</u>	0.99	−0.93	1.32824	1.29	
71	0.95	0.03	0.69	0.06	1346.10	868.22		0.00	0.00	−1.38	1.26427	−1.38	
72	0.88	0.02	0.51	0.04	938.92	130.99		0.00	0.00	−0.60	0.80274	−0.60	
73	0.91	0.04	0.85	0.04	470.17	156.41		0.00	0.00	0.17	1.10142	0.17	
74	0.941	0.04	0.85	0.04	595.88	194.03		0.00	0.00	−0.25	1.73365	−0.25	
75	0.871	0.03	0.66	0.05	1093.18	246.01		0.00	0.00	<u>9.99</u>	1.0553	<u>9.99</u>	>70
76	1.001	0.00	0.70	0.05	10.90	4.73	*	<u>5.27</u>	1.17	<u>11.36</u>	1.35699	<u>16.56</u>	>70
77	0.961	0.03	0.92	0.04	760.79	906.62		0.00	0.00	1.32	1.12398	1.32	

S^2, τ_e and R$_{ex}$ have been deduced from a Modelfree analysis (A. Palmer, Columbia University). R$_{ex}$ values higher than 1.5 Hz, which corresponds to the maximal error, are underlined. The asterisks in the J(0) column indicate residues corresponding to experimental points located out of the allowed light blue region in Figure 4a. R$_2$−R$_{1\rho}$(90°) values higher than 2.5 Hz are also underlined (the maximal error is 2.08 Hz). The column 'Var' contains the sum of R$_{ex}$ and R$_2$−R$_{1\rho}$(90°), and thus corresponds to the amplitude of the R$_{1\rho}$(90°) variations as a function of ω_{eff}. Because of the experimental errors, the fit of R$_{1\rho}$(90°) as a function of ω_{eff} was carried out only when the Var parameter was higher than 4 Hz (underlined). The last two columns contain the exchange time scales measured for the C$_\alpha$H and NH bonds, respectively. Here, underlined values indicate the exchange correlation times measured for both the C$_\alpha$H and NH bonds.

was performed by comparing the ^{13}C R$_2$ derived from the line widths in the reference experiment (Figure 1a) to the ^{13}C R$_{1\rho}$ (90°), and by analyzing the dependency of the ^{13}C R$_{1\rho}$ (90°) value upon the rf irradiation strength.

Figure 7a displays the comparison of the ^{13}C R$_2$, corresponding to the reference line widths, with the mean ^{13}C R$_{1\rho}$ (90°). Differences higher than 4 Hz are found for Q7 and S9 in loop 1, N22, W28, I36, E37, R38 in loop 2, and P43, T44 (α,β), V45, K46, P47, I49, L51, N52, C54 and T55 (α,β) in loop 3. Thus, the C$_\alpha$ or C$_\beta$ sites of these residues are subject to μs to ms time scale motions. A measurable R$_{ex}$ was already found for 11 of these in the preceding analysis (Table 1). For the remaining residues, the fast exchange contribution to relaxation appears to be filtered out of the R$_{1\rho}$ (90°) values. The correlation time of the corresponding motions is thus longer than about 70 μs.

To better define the correlation time of the motions on the μs to ms time scale, R$_{1\rho}$ (90°) values of each studied ^{13}C were plotted as a function of the rf field strength (Figure 7b). The intrinsic line width R$_2$, measured under ^{1}H irradiation, was used as an R$_{1\rho}$ (90°)

value at ω_{eff} = 0. Moreover, the R$_{1\rho}$ (90°) −R$_{ex}$ value deduced from Modelfree was used as R$_2^{DD,CSA}$. Under these conditions, we could derive a restricted range for each exchange correlation time (Table 1), but the apparent precision mostly relies on the fixed R$_2^{DD,CSA}$ so that we analysed the obtained results from a rather qualitative point of view, considering groups of residues within a shared range (Figure 7c). A time scale of 30 to 90 μs was observed for C$_\alpha$ of residues S8, S9 (loop 1), W28 (loop 2), K46 (loop 3) and T56 (C-terminal turn) (in red in Figure 7c). Exchange for these residues corresponds to chemical shift differences lower than 1 ppm. A time scale of 50 μs to 10 ms was found for C$_\alpha$ of residues H4, T14 (loop 1) and T21 (turn between loops 1 and 2) (in orange in Figure 7c). Finally, carbons exhibiting an exchange correlation time higher than 70 μs were divided into those showing an R$_2$−R$_{1\rho}$ (90°) value lower or higher than 10 Hz (in yellow or green, respectively, in Figure 7c). Carbons belonging to the latter category exhibit either particularly high chemical shift differences, or particularly slow motions, unless the equilibrium distribution of the population in exchange is very different (closer to a 1:1 distribution) for the green carbons compared to
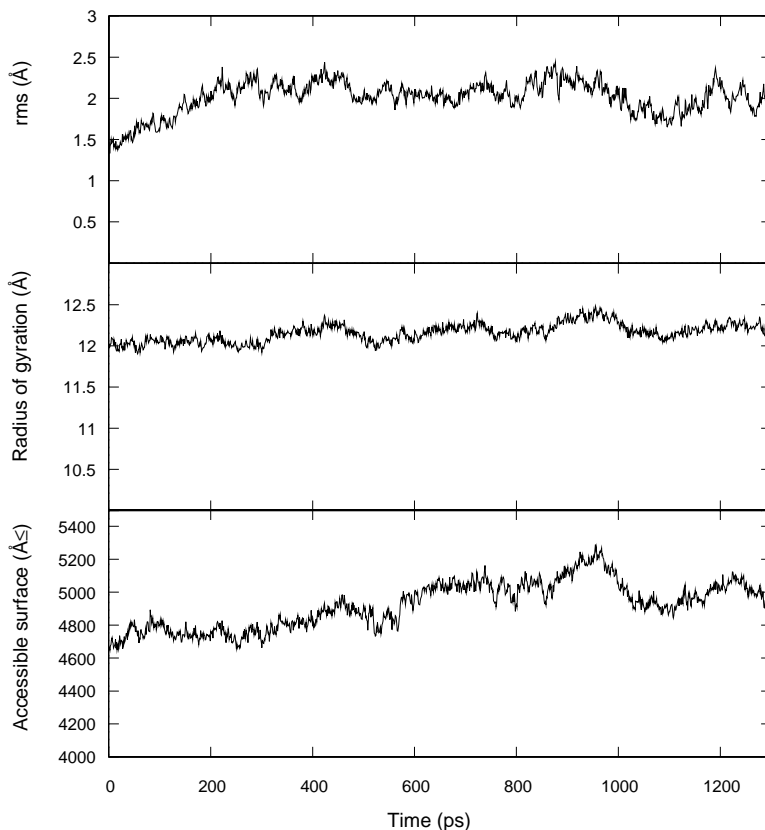
60

Figure 9. Variations of (a) the rms deviation to the original structure, (b) the radius of gyration, and (c) the accessible surface of toxin α during the 1.3 ns simulation.

the yellow ones. Interestingly, whereas more than half of the yellow carbons is located in loop 2, the green carbons are found in loop 3 (Figure 7c).

Finally, two C_β show an exchange correlation time higher than 70 μs, and an $R_2-R_{1\rho}$ (90°) difference higher than 10 Hz. The C_α corresponding to these residues, i.e. T44 and T55, exhibit the same properties.

Comparison of the ^{15}N and ^{13}C relaxation data

The generalized order parameters S^2 related to the ps to ns motions of NH and CH backbone vectors are plotted in Figure 8. Variation of both order parameters as a function of the protein sequence is globally the same, high amplitude fast motions being found at the tips of loops 1 and 2 (S9 in loop 1, R29–R32 in loop 2), in the turn linking loops 1 and 2 (T21) and in the external part of loop 3 (P43–P47). Rigid parts of the protein approximately correspond in both cases to the β-sheet structure (Guenneugues et al., 1997; Figure 8).

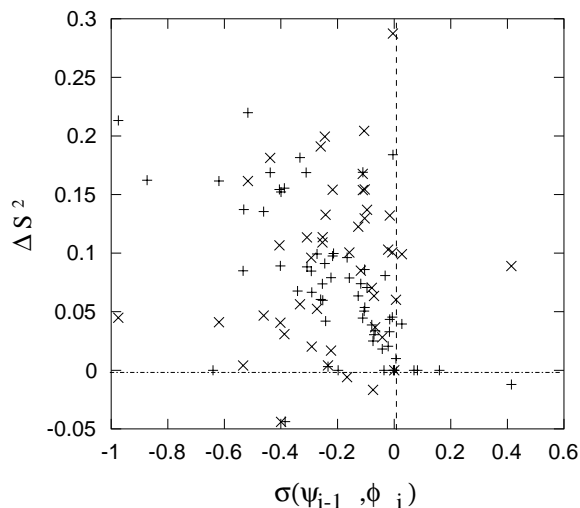A detailed study of the μs to ms time scale motions of backbone nitrogen nuclei in toxin α (Zinn-Justin

Figure 10. Correlation plot of the NH and $C_\alpha H_\alpha$ order parameter differences (diamonds and crosses refer to S^2 extracted from the NMR data and from the simulation, respectively) and the values of the cross-correlation functions for the fluctuations of torsion angles Ψ_{i-1} and Φ_i at 0.5 ps.
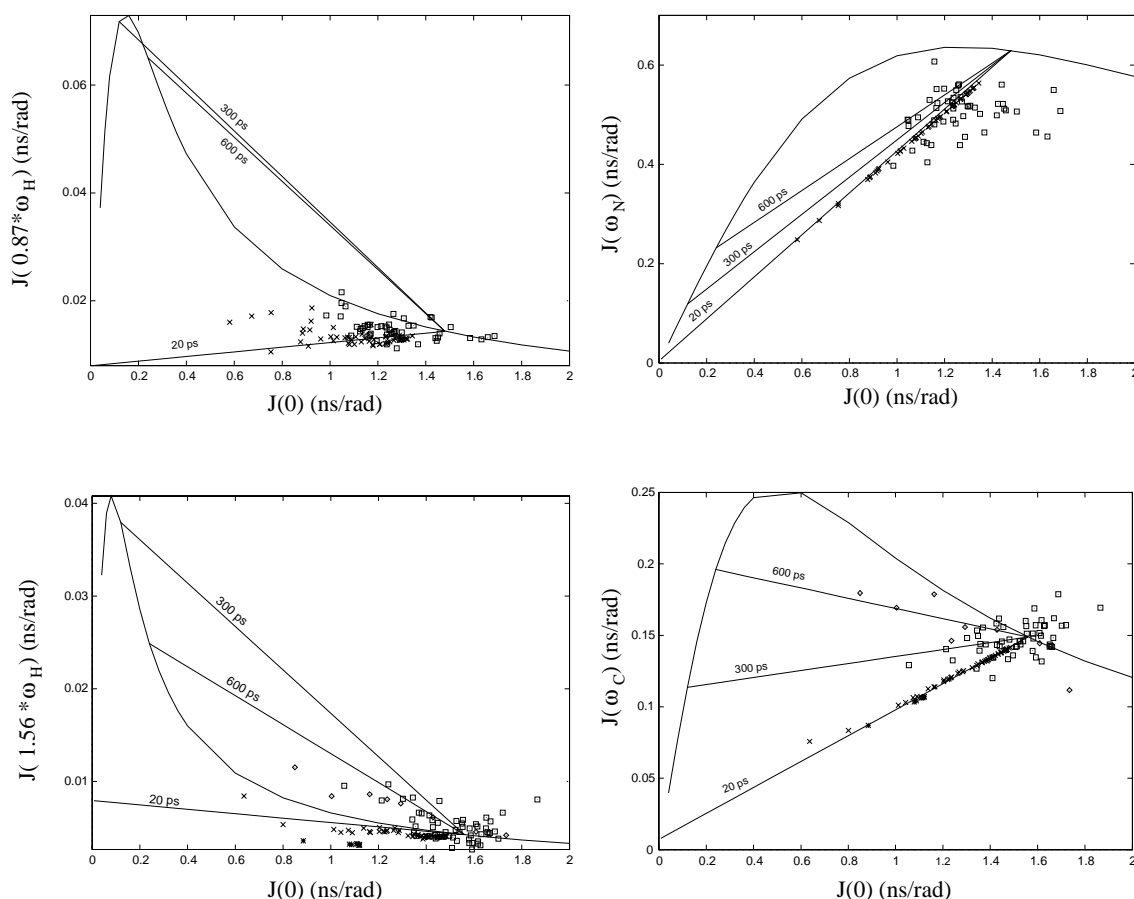
Figure 11. Comparison of the spectral density values deduced from the NMR data (backbone ^{15}N and ^{13}C$_\alpha$ in squares, threonine ^{13}C$_\beta$ in diamonds) and from the simulation (backbone ^{15}N and ^{13}C$_\alpha$ in crosses, threonine ^{13}C$_\beta$ in stars). The curves and straight lines are those displayed in Figure 4.

et al., 1997) showed that C3, N5, S9 (loop 1), C17, E20, T21 (turn between loops 1 and 2), and K26 and I35 (loop 2) exhibit motions with a correlation time of 1 to 250 μs, whereas the correlation times of T44, G48, K50 (loop 3) and K58 (C-terminal loop) are longer than 1 ms. Thus, for four residues (S9, T21, T44 and L51), the exchange correlation time has been evaluated on the NH and the C$_\alpha$H bonds, giving consistent results (Table 1).

Validation of the simulation on the basis of the ^{15}N and ^{13}C NMR data

The fluctuations of the temperature, the radius of gyration and the rms deviation to the starting structure indicate a good stability of the protein during the 1.3 ns of the simulation (Figure 9). The increase in the rms deviation to the average NMR structure is due to a slight displacement of residues P18 and K58 which

induces no significant increase of the accessible surface nor of the radius of gyration. Further analysis was performed over the 0.3 to 1.3 ns part of the trajectory.

The autocorrelation functions for the backbone NH and C$_\alpha$H$_\alpha$ vectors can roughly be sorted into three classes. In class I, the correlation function reaches a plateau value in less than 20 ps and essentially gathers residues belonging to rigid parts of the protein. In class II, the correlation function reaches a plateau value, but within more than 20 ps. The residues concerned are located in less rigid parts of the molecule. In class III, no plateau value is reached. The corresponding residues are located at the tips of the loops, that is, in the most mobile parts of the protein. Out of the 55 NH correlation functions, 29 belong to class I, 17 to class II and 9 (S9, G19, H31, R32, G33, T34, V45, I49 and N61) to class III. Among the 56 C$_\alpha$H$_\alpha$ correlation functions, 42 belong to class I, 9 to class II

and 6 (S9, P11, T44, V45, P47 and N61) to class III. Four class III correlation functions involve glycine or proline residues for which only one function (corresponding to NH or $C_\alpha H_\alpha$) can be computed. For S9, V45 and N61 both correlation functions belong to class III. For three residues, the class III NH correlation functions correspond to class II $C_\alpha H_\alpha$ correlation functions. In one case only (T34), the NH and $C_\alpha H_\alpha$ correlation functions belong to very different classes.

Figure 8 displays the comparison between the generalized order parameter S^2 of backbone NH and $C_\alpha H_\alpha$ derived from experimental data or computed over the simulation. The latter were calculated using either a mono- or bi-exponential fitting of the autocorrelation function. Except for most of the class III autocorrelation functions, both fitting procedures gave an identical value of the order parameter. Similarly to the values computed out of NMR relaxation rates, the variation of the order parameters extracted from the simulation along the protein sequence is correlated with the secondary structure. The values of S^2 are higher in the β-strands than in the loops, and the highest are in the central loop.

Only four NH S^2 values differ by more than 0.2 from the corresponding NMR values. The correlation functions of these four vectors (S9, G19, G33, V45) belong to class III and therefore did not reach any plateau value. In order to analyse the movement of the corresponding NH bond vectors, the scalar products with the original vectors were calculated. This analysis shows unfrequent large reorientations of the NH vectors along the simulation. Such rare movements correspond to large variations of the Ψ and Φ angles (>60°). Their occurrence precludes the calculation of a reliable order parameter. Furthermore, for five residues (N5, Q6, S8, Q10 and K58), the order parameters differ by more than 0.1 and less than 0.2 from the corresponding NMR-derived value. These residues all belong to class II. The backbone dihedral angles of these residues also present rare transitions but with lower amplitude (<60°). For 5 residues (H31, R32, T34, I49 and N61), although the correlation functions belong to classs III, the value of the order parameter derived using the fitting procedure is unexpectedly in agreement with the experimental one.

In the case of the backbone $C_\alpha H_\alpha$ vectors, the S^2 values of residues S9 and R32 differ by 0.2 from the corresponding NMR values. The S9 $C_\alpha H_\alpha$ vector presents a transition from a constrained to a non-constrained position at 300 ps and the R32 $C_\alpha H_\alpha$ vector displays only one large transition at 700 ps. By
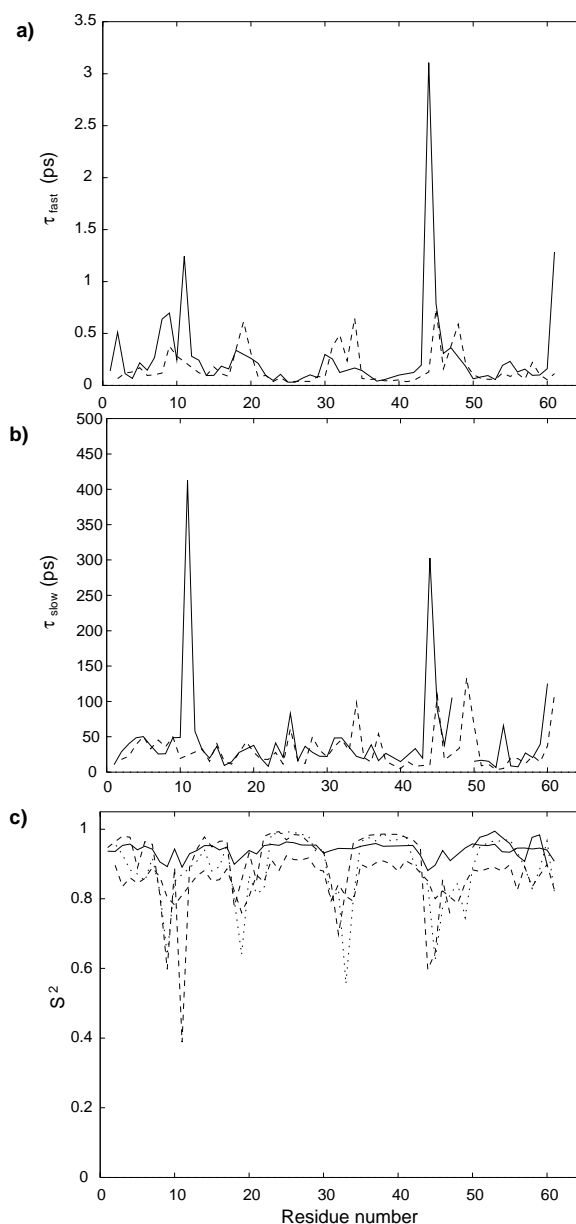

Figure 12. Correlation times and amplitudes of the backbone NH and $C_\alpha H_\alpha$ motions observed in the simulation, as a function of the sequence. The correlation times of the NH and $C_\alpha H_\alpha$ motions of the (a) fastest and (b) slowest observed motions are displayed in solid and dashed lines, respectively. Amplitudes are displayed according to the following code: solid lines, longer dashed lines, shorter dashed lines and dotted lines refer to the order parameters of the slowest motions of $C_\alpha H_\alpha$, the fastest motions of $C_\alpha H_\alpha$, the slowest motions of NH and the fastest motions of NH vectors, respectively.

removing the effect of this transition, the S^2 value for R32 increases from 0.7 to 0.8. The four other residues for which the S^2 value differs by more than 0.1 as compared to the NMR value are S8, P18, P47 and I49. As for the NH vectors, the difference between the NMR and simulated $C_\alpha H_\alpha$ order parameters is due to the presence of unfrequent reorientations of the $C_\alpha H_\alpha$ vector, precluding the calculation of a reliable order parameter.

In both the experimental and simulated cases, the order parameters of the $C_\alpha H_\alpha$ vectors are higher than those of the NH vectors. A particularly high freedom around the axis joining two successive C_α was recently shown for the NH and CO bonds of the peptidic plane (Lienin et al., 1998). This was described in simulations as anti-correlated fluctuations of the torsion angles Ψ_{i-1} and Φ_i (Fadel et al., 1995). This is also observed in our simulated trajectory (Figure 10), but is less obvious for the parameters extracted from the experimental data. However, as the fast motions simulated by molecular dynamics are consistent with the measured NMR parameters, we think that this explanation still stands. Probably, the errors made on the order parameters derived from experimental data being relatively important, the correlation between Ψ,Φ angle variations is difficult to obtain. As already stressed in the literature (Philippopoulos et al., 1997), molecular dynamics simulations enable to determine order parameters for fast motions with a higher precision than those originating from NMR measurements, which is a critical advantage for the observation of some detailed properties of protein motions.

Comparison of the spectral density distributions calculated from the NMR experiments and from the simulation

Figure 11 reports the spectral density values extracted from the experiment and from the simulation, on a $J(\omega)$ as a function of $J(0)$ plot. The observed distributions are noticeably different. Molecular dynamics essentially samples motions on a time scale up to 20 ps, as shown by the linear distribution of the data points resulting from the simulation. On the graphs displaying spectral densities at the frequencies affecting ^{15}N relaxation, the experimental data points are translated to higher $J(0)$ values compared to the simulated ones. This suggests that the main difference between the experiment and the simulation arises from the μs to ms motions. Nevertheless, in the diagrams reporting the spectral densities at frequencies affecting ^{13}C relaxation, the experimental data points are

not only translated horizontally relatively to the simulated points, but are also found above the simulated data points. This is due to the motions in the 0.1–1 ns range affecting the NMR-derived parameters as shown previously ; these motions are not sampled in a proper way during the 1 ns simulation.

The motions observed along the simulation may be classified according to their time scale:
- The fastest ones are subpicosecond, and their correlation time varies as a function of the secondary structure (Figure 12a). They are responsible for the first fast decay of the correlation functions (the 'initial drop'; Fushman et al., 1994), and are linked to harmonic oscillations like the 'librational motions' of the NH bond out of the peptidic plane (Fushman et al., 1994).
- Then, motions with a time scale of about 20 ps are found. They correspond to Φ,Ψ angle fluctuations. Analysis of the simulation does not show any dependence of the correlation time of these motions with the secondary structure (Figure 12b), probably because correlation times higher than 50 ps are not sampled properly.
- Finally, infrequent transitions are found. They correspond to motions with a correlation time higher than 100 ps. Whether they are related to the experimentally evidenced slower motions or are simply artefactual is not possible to discriminate in the present study, since this will require new or longer simulations.

The order parameters computed along the trajectory are thus the product of two order parameters, one corresponding to the subpicosecond motions, and the other to the 20 ps motions. The third type of motion causes errors in the proper evaluation of S^2, because of insufficient sampling. Interestingly, the regions involved in higher amplitude motions are the same, whatever the time scale; the longer the time scale, the higher the amplitudes (Figure 12c). This is particularly encouraging: it means that the variations of S^2 extracted from NMR data by taking into account a single internal correlation time are conserved whatever the time scale. It also means that the motions influencing at most the τ_e value are the slowest ones. An important restriction to these considerations has to be stressed: we have no data yet on simulated motions with a correlation time longer than 100 ps. Will the amplitudes of such motions vary as the amplitudes of the fastest ones?

Comparison with the structural variations observed in high resolution crystal structures for proteins highly analogous to toxin α, erabutoxins a and b

Toxin α has 73% sequence similarity to erabutoxins a and b from *Laticauda semifasciata*. The crystal structures of these proteins have been determined under various conditions (Low et al., 1976; Tsernoglou and Petsko, 1976; Smith et al., 1988; Corfield et al., 1989; Saludjian et al., 1992; Arnoux et al., 1994; Nastopoulos et al., 1998). Interestingly, multiple conformers are a common feature of the erabutoxin crystal structures. Indeed, in the 2.0 Å Ea model (PDB code 5EBX; Corfield et al., 1989), two side chains were modelled as alternate conformers. In the recent 1.5 Å resolution structure of Ea, 6 and 11 residues were found to be bimodal in the monomeric and dimeric form, respectively (PDB codes 1QKE and 1QKD; Nastopoulos et al., 1998). At 1.4 Å resolution, in the monomeric form of Eb (PDB code 3EBX; Smith et al., 1988), 15 residues were found to be bimodal. More precisely, in Ea and Eb monomeric forms, residues with alternate positions are located at the tip of loop 1 (S9, the numbering referring to the toxin α sequence), at the tip of loop 2 (R32), in loop 2 (E37), in the C-terminal turn (T55, S56) and at the C-terminus (N61), i.e. in regions showing experimentally a high flexibility in toxin α. Furthermore, in Eb, an additional region, corresponding to the external part of loop 3 (P43 to K50), shows two possible conformations. This region, together with S9, E37 and the T55 to S56 segment, shows important μs to ms time scale motions in toxin α (Figure 7c, Table 1).

Conclusions

Backbone NH and CH fast (ps-ns) motion amplitudes

In toxin α, both experimental and simulated $C_\alpha H_\alpha$ order parameters are higher than the corresponding NH S^2. This was already described in the case of BPTI (Smith et al., 1995) and human transforming growth factor (Fadel et al., 1995). Smith et al. (1995) concluded that the NH vectors, as opposed to $C_\alpha H_\alpha$ vectors, can display a higher degree of motional freedom, the rotation of an intact amide group around the bonds connecting it to adjacent carbons inducing little disturbance to the rest of the structure. Similarly, Fadel et al. (1995) proposed that anti-correlated motions of adjacent backbone dihedral angles led to such an S^2 difference. In our simulation, differences between $C_\alpha H_\alpha$ and NH S^2 can indeed be attributed, at least partially, to anti-correlated variations of the torsion angles Ψ_{i-1} and Φ_i (Figure 10). Interestingly, in the case of mellitin, similar $C_\alpha H_\alpha$ and NH S^2 of about 0.5 were measured in the monomeric random-coil state, while in the 'primarily α-helical, protein-like tetramer', NH S^2 were found to be higher than $C_\alpha H_\alpha$ S^2 (Zhu et al., 1998). Thus, having $C_\alpha H_\alpha$ order parameters higher than the NH ones might be characteristic of well-structured and stable proteins.

Microsecond–millisecond time scale motions

More than half of the toxin backbone appears to exhibit observable μs to ms time scale motions. ^{15}N and ^{13}C relaxation studies indicate consistent exchange time scales for the 4 residues S9, T21, T44 and L51. For 27 other residues, either the NH or the $C_\alpha H$ exhibited observable μs to ms motions. Interestingly, most of loop 3 shows particularly large amplitude or slow motions on a time scale higher than 70 μs, and this loop also exhibits conformational disorder in a toxin highly analogous to toxin α, erabutoxin b (Smith et al., 1988).

At first view, it may seem surprising that toxin α, which is a highly stable protein (melting temperature of 75 °C; Thai and Leonetti, personal communication), exhibits this type of motions on more than half of its structure. However, lifetime determinations of water molecules by Denisov and Halle (1995), residual dipolar coupling measurements by Tolman et al. (1997), and a study of μs conformational fluctuations in the third fibronectin type III domain by Akke et al. (1998) suggested that significant μs to ms time scale motions may well be a general feature of protein dynamics. Moreover, Muñoz et al. (1997) have shown that a β-hairpin can fold in a few microseconds. Thus, μs to ms time scale motions in a β-structure as that of toxin α could reflect partial unfolding events.

Is the functional site of toxin α particularly mobile?

Localisation of the nicotinic acetylcholine receptor binding site of Ea has been probed by mutagenesis analysis (Pillet et al., 1993; Trémeau et al., 1995). Ten residues are involved in the functional site of erabutoxin a. All ten residues are present in toxin α, suggesting that the functional site of toxin α is similar to that of Ea. These residues are Q7, S8 and Q10 at the tip of loop 1, K26, W28, D30, R32 and E37 in loop 2 and K46 in loop 3. Interestingly, the amplitude of the backbone ps-ns time scale motions of the functional residues is distributed over the whole observed S^2 range. Furthermore, these residues are subject to μs to

ms time scale motions as most of the molecule. Thus, the functional site of toxin α is not more flexible than the rest of the molecule, although its flexibility might nevertheless be critical for the binding to its target. The particularly long residence time of the toxin on the receptor (several days) might be achieved through a plasticity allowed by the mentioned motions.

Experience and simulation

Comparison of the experimental and simulated data pointed out that additional motions with correlation times longer than 100 ps contribute to the NMR relaxation data. These motions are particularly important in the case of $C_\beta H_\beta$ vectors of threonines. The presence of motions on the μs to ms time scale for more than half of the studied carbon nuclei in the toxin makes it difficult to extract the correlation times of the fast motions out of the experimental data. In particular, it is not possible to derive a shared correlation time in the 0.1–4 ns range for all $C_\alpha H_\alpha$ vectors (Lefèvre et al., 1996; van Heijenoort et al., 1998). A longer simulation is needed in order to describe the motions on this time scale. In addition, such a simulation will allow the validation of models used to describe the spectral density functions of NH and CH vectors.

Acknowledgements

References

Akke, M., Skelton, N.J., Kordel, J., Palmer, A.G. III and Chazin, W.J. (1993) *Biochemistry*, **32**, 9832–9844.

Akke, M., Liu, J., Cavanagh, J., Erickson, H.P. and Palmer, A.G. (1998) *Nat. Struct. Biol.*, **5**, 55–59.

Arnoux, B., Ménez, R., Drevet, P., Boulain, J.-C., Ducruix, A. and Ménez, A. (1994) *FEBS Lett.*, **342**, 12–14.

Banci, L., Bertini, I., Cavazza, C., Felli, I.C. and Koulougliotis, D. (1998) *Biochemistry*, **37**, 12320–12330.

Barbato, G., Ikura, M., Kay, L.E., Pastor, R.W. and Bax, A. (1992) *Biochemistry*, **31**, 5269–5278.

Beeser, S.A., Goldenberg, D.P. and Oas, T.G. (1997) *J. Mol. Biol.*, **269**, 154–164.

Bodenhausen, G. and Ruben, D. (1980) *Chem. Phys. Lett.*, **69**, 185–189.

Bodenhausen, G. and Ernst, R.R. (1981) *J. Magn. Reson.*, **45**, 367–373.

Brooks, B.R., Bruccoleri, R.D., Olafson, B.O., States, D.J., Swaminathan, S. and Karplus, M. (1983) *J. Comput. Chem.*, **4**, 187–217.

Brooks III, C.L., Karplus, M. and Pettit, B.M. (1988) *Proteins: A theoretical Perspective of Dynamics, Structure and Thermodynamics*, Adv. in Chem. Phys. LXXI, Wiley, New York, NY.

Cavanagh, J., Palmer III, A.G., Wright, P. and Rance, M. (1991) *J. Magn. Reson.*, **91**, 429–436.

Cavanagh, J. and Rance, M. (1993) *Annu. Rep. NMR Spectrosc.*, **27**, 1–58.

Clore, G.M., Szabo, A., Bax, A., Kay, L.E., Driscoll, P.C. and Gronenborn, A.M. (1990) *J. Am. Chem. Soc.*, **112**, 4989–4991.

Corfield, P.W.R., Lee, T.-J. and Low, B.W. (1989) *J. Biol. Chem.*, **264**, 9239–9242.

Davis, A.L., Keeler, J., Laue, E.D. and Moskau, D. (1992) *J. Magn. Reson.*, **98**, 207–216.

Denisov, V.P. and Halle, B. (1995) *J. Mol. Biol.*, **245**, 682–697.

Desvaux, H., Birlirakis, N., Wary, C. and Berthault, P. (1995) *Mol. Phys.*, **86**, 1059–1073.

Deverell, C., Morgan, R.E. and Strange, J.H. (1970) *Mol. Phys.*, **18**, 553–559.

Engelke, J. and Rüterjans, H. (1998) *J. Biomol. NMR*, **11**, 165–183.

Fadel, A.R., Jin, D.Q., Montelione, G.T. and Levy, R.M. (1995) *J. Biomol. NMR*, **6**, 221–226.

Farrow, N.A., Zhang, O., Szabo, A., Torchia, A. and Kay, L.E. (1995) *J. Biomol. NMR*, **6**, 153–162.

Fischer, M.W.F., Zeng, L., Pang, Y., Hu, W., Majumdar, A. and Zuiderweg, E.R.P. (1997) *J. Am. Chem. Soc.*, **119**, 12629–12642.

Fryklund, L. and Eaker, D. (1975) *Biochemistry*, **14**, 2865–2871.

Fushman, D., Ohlenschläger, O. and Rüterjans, H. (1994) *J. Biomol. Struct. Dyn.*, **11**, 1377–1402.

Garcia de la Torre, J. and Bloomfield, V.A. (1981) *Q. Rev. Biophys.*, **14**, 81–139.

Gesmar, H., Led, J.J. and Abilgaard, F. (1990) *Prog. NMR Spectrosc.*, **22**, 255–288.

Guenneugues, M., Drevet, P., Pinkasfeld, S., Gilquin, B., Ménez, A. and Zinn-Justin, S. (1997) *Biochemistry*, **36**, 16097–16108.

Ishima, R., Yamasaki, K., Saito, M. and Nagayama, K. (1995) *J. Biomol. NMR*, **6**, 217–220.

Jorgensen, W.L. (1981) *J. Am. Chem. Soc.*, **103**, 335–340.

Low, B.W., Preston, H.S., Sato, A., Rosen, L.S., Searl, J.E., Rudko, A.D. and Richardson, J.S. (1976) *Proc. Natl. Acad. Sci. USA*, **73**, 2991–2994.

Kay, L.E., Keifer, P. and Saarinen, T. (1992) *J. Am. Chem. Soc.*, **114**, 10663–10665.

Kay, L.E. (1998) *Nat. Struct. Biol.*, **5**, 513–517.

Kay, L.E., Muhandiram, D.R., Wolf, G., Shoelson, S.E. and Forman-Kay, J.D. (1998) *Nat. Struct. Biol.*, **5**, 156–163.

Lee, L.K., Rance, M., Chazin, W.J. and Palmer, A.G. (1997) *J. Biomol. NMR*, **9**, 287–298.

Lefèvre, J.-F., Dayie, K.T., Peng, J.W. and Wagner, G. (1996) *Biochemistry*, **35**, 2674–2686.

LeMaster, D.M. and Kushlan, D.M. (1996) *J. Am. Chem. Soc.*, **118**, 9255–9264.

Lienin, S.F., Bremi, T., Brutscher, B., Bruschweiler, R. and Ernst, R.R. (1998) *J. Am. Chem. Soc.*, **120**, 9870–9879.

Lipari, G. and Szabo, A. (1982a) *J. Am. Chem. Soc.*, **104**, 4546–4559.

Lipari, G. and Szabo, A. (1982b) *J. Am. Chem. Soc.*, **104**, 4559–4570.

Loncharich, R.J. and Brooks, B.R. (1989) *Proteins Struct. Funct. Genet.*, **6**, 32–45.

MacKerell, A.D., Bashford, D., Bellott, M., Dunbrack, R.L., Evanseck, J.D., Field, M.J., Fischer, S., Gao, J., Guo, H., Ha, S., Joseph-McCarthy, D., Kuchnir, L., Kuczera, K., Lau, F.T.K., Mattos, C., Michnick, S., Ngo, T., Nguyen, D.T., Prodhom, B., Reiher, W.E., Roux, B., Schlenkrich, M., Smith, J.C., Stote, R., Straub, J., Watanabe, M., Wiorkiewicz-Kuczera, J., Yin, D. and Karplus, M. (1998) *J. Phys. Chem.*, **B102**, 3586–3616.

Mandel, A.M. and Palmer III, A.G. (1994) *J. Magn. Reson.*, **A110**, 62–72.

Marion, D., Ikura, M., Tschudin, R. and Bax, A. (1989) *J. Magn. Reson.*, **85**, 393–399.

Muñoz, V., Thompson, P.A., Hofrichter, J. and Eaton, W.A. (1997) *Nature*, **390**, 196–199.

Nastopoulos, V., Kanellopoulos, P.N. and Tsernoglou, D. (1998) *Acta Crystallogr.*, **D54**, 964–974.

Nicholson, L.K., Kay, L.E., Baldisseri, D.M., Arango, J., Young, P.E., Bax, A. and Torchia, D.A. (1992) *Biochemistry*, **31**, 5253–5263.

Otting, G. and Wüthrich, K. (1988) *J. Magn. Reson.*, **76**, 569–574.

Palmer III, A.G., Cavanagh, J., Wright, P.E. and Rance, M. (1991a) *J. Magn. Reson.*, **93**, 151–170.

Palmer III, A.G., Rance, M. and Wright, P.E. (1991b) *J. Am. Chem. Soc.*, **113**, 4371–4380.

Palmer III, A.G. (1993) *Curr. Opin. Biotechnol.*, **4**, 385–391.

Peng, J.W. and Wagner, G. (1992a) *Biochemistry*, **31**, 8571–8586.

Peng, J.W. and Wagner, G. (1992b) *J. Magn. Reson.*, **98**, 308–332.

Philippopoulos, M., Mandel, A.M., Palmer III, A.G. and Lim, C. (1997) *Proteins Struct. Funct. Genet.*, **28**, 481–493.

Pillet, L., Trémeau, O., Ducancel, F., Drevet, P., Zinn-Justin, S., Pinkasfeld, S., Boulain, J.-C. and Ménez, A. (1993) *J. Biol. Chem.*, **268**, 909–916.

Richarz, R., Nagayama, K. and Wüthrich, K. (1980) *Biochemistry*, **19**, 5189–5196.

Rischel, C., Madsen, J.C., Andersen, K.V. and Poulsen, F.M. (1994) *Biochemistry*, **33**, 13997–14002.

Ryckaert, J.-P., Ciccotti, G. and Berendsen, H.J.C. (1977) *J. Comput. Phys.*, **23**, 327–341.

Saludjian, P., Prangé, T., Navaza, J., Ménez, R., Guilloteau, J.P., Riès-Kautt, M. and Ducruix, A. (1992) *Acta Crystallogr.*, **B48**, 520–531.

Schleucher, J., Schwendiger, M., Sattler, M., Schmidt, P., Schedletzky, O., Glaser, S.J., Sørensen, O.W. and Griesinger, C. (1994) *J. Biomol. NMR*, **4**, 301–306.

Shaka, A.J., Keeler, J. and Freeman R. (1983) *J. Magn. Reson.*, **53**, 313–340.

Shaka, A.J., Barker, P.B. and Freeman, R. (1985) *J. Magn. Reson.*, **64**, 547–552.

Smith, J.L., Corfield, P.W.R., Hendrickson, W.A. and Low, B.W. (1988) *Acta Crystallogr.*, **A44**, 357–368.

Smith, P.E., van Schaik, R.C., Szyperski, T., Wüthrich, K. and van Gunsteren, W.F. (1995) *J. Mol. Biol.*, **246**, 356–365.

Szyperski, T., Luginbühl, P., Otting, G., Güntert, P. and Wüthrich, K. (1993) *J. Biomol. NMR*, **3**, 151–164.

Tjandra, N., Kuboniwa, H., Ren, H. and Bax, A. (1995a) *Eur. J. Biochem.*, **15**, 1014–1024.

Tjandra, N., Feller, S.E., Pastor, R.W. and Bax, A. (1995b) *J. Am. Chem. Soc.*, **117**, 12562–12566.

Tolman, J.R., Flanagan, J.M., Kennedy, M.A. and Prestegard, J.H. (1997) *Nat. Struct. Biol.*, **4**, 292–297.

Trémeau, O., Lemaire, C., Drevet, P., Pinkasfeld, S., Ducancel, F., Boulain, J.-C. and Ménez, A. (1995) *J. Biol. Chem.*, **270**, 9362–9369.

Tsernoglou, D. and Petsko, G. (1976) *FEBS Lett.*, **68**, 1–4.

van Heijenoort, C., Penin, F. and Guittet, E. (1998) *Biochemistry*, **37**, 5060–5073.

Venable, R.M. and Pastor, R.W. (1988) *Biopolymers*, **27**, 1001–1014.

Wand, A.J., Urbauer, J.L., McEvoy, R.P. and Bieber, R.J. (1996) *Biochemistry*, **35**, 6116–6125.

Wong, K.-B. and Daggett, V. (1998) *Biochemistry*, **37**, 11182–11192.

Wüthrich, K., Wagner, G., Richarz, R. and Braun, W. (1980) *Biophys. J.*, **32**, 549–560.

Zhu, L., Prendergast, F.G. and Kemple, M.D. (1998) *J. Biomol. NMR*, **12**, 135–144.

Zinn-Justin, S., Roumestand, C., Gilquin, B., Bontems, F., Ménez, A. and Toma, F. (1992) *Biochemistry*, **31**, 11335–11347.

Zinn-Justin, S., Berthault, P., Guenneugues, M. and Desvaux, H. (1997) *J. Biomol. NMR*, **10**, 363–372.